Large-scale inverted-V channels of upflowing oxygen ions pumped by Alfvén waves

Hui Zhang[1,2,3]*, Jun Zhong[1,2,3], SuiYan Fu[4], ZuYin Pu[4], Yong Wei[1,2,3], Lun Xie[4], LiBo Liu[1,2,3], and QiAn Chen[4]

[1]Key Laboratory of Earth and Planetary Physics, Institute of Geology and Geophysics, Chinese Academy of Sciences, Beijing 100029, China;

[2]College of Earth Sciences, University of Chinese Academy of Sciences, Beijing 100049, China;

[3]Heilongjiang Mohe National Observatory of Geophysics, Institute of Geology and Geophysics, Chinese Academy of Sciences, Beijing 100029, China;

[4]School of Earth and Space Sciences, Peking University, Beijing 100871, China

Abstract: Large-scale inverted-V channels of upflowing oxygen ions are frequently identified in data collected by Cluster, at all local times, near the open-closed field line boundary over Earth's high-latitude ionosphere-occur with downward propagating MHD Alfvén waves which have cascaded into kinetic regimes of plasma. The transverse acceleration of the oxygen ions in the center of these structures is interpreted as the integrated energization by these waves along the channels. Also observed within the channels are upward parallel electric fields, a key characteristic of kinetic Alfvén waves, which may contribute not only to lifting the ions but also to precipitating aurora electrons that might initiate ion upflow in the ionosphere below. Statistics on five-year observations of Cluster show that the channels typically form during geomagnetic perturbations, particularly when solar-wind dynamic pressure is high or highly fluctuated. Near the open-closed field line boundary, the stronger the wave power, the higher the upward oxygen flux and the higher the beam energy, indicating that these waves provide a simple but efficient way to drive oxygen upflows.

Keywords: oxygen ions; dispersive Alfvén waves; ion outflow; parallel electric field

1. Introduction

Since realizing that the Earth's ionosphere is a plasma source of the planet's magnetosphere (Axford, 1968), the ionosphere-origin plasma, distinctively characterized by the presence of oxygen ions (O^+), has been revealed to be scattered to every corner of the magnetosphere (Young, 1986; Kronberg et al., 2014), in which it causes global perturbations (Yau and André, 1997). Unlike the light-ion species (H^+ and He^+), the heavy O^+ ions are bound more tightly to the Earth and are harder to escape from the Earth unless additional acceleration occurs. High-latitude regions of the ionosphere, particularly the cusp/cleft regions, are the main outlets for this escape (Shelley et al., 1982; Chappell, 1988), where the geomagnetic fields are dominantly vertical and exert less magnetic constraint against the lifting of heavy and cold ionospheric ions. A field-aligned ambipolar electric field, typically deriving from the buoyant force of heated electrons in the top of the ionosphere, is a natural candidate to initiate O^+ upflows (Axford, 1968); the required energy is carried by either downward propagating waves or by precipitating electrons (Strangeway et al., 2005; Brambles et al., 2011; Zhao K et al., 2020).

After that, many mechanisms are thought to accelerate the

upflowing cold heavy O^+ ions sequentially at different altitudes, as a relay race team, and to lift these ions up step by step into the magnetosphere. Early rocket exploration, however, found many transversely-accelerated ion (TAI) events, instead of field-aligned ion beams, at the lower altitudes above the ionosphere, indicating that the accelerations are primarily in the perpendicular direction. A variety of waves — electrostatic (e.g., the electrostatic ion cyclotron wave (EIC) and the low hybrid wave (LH)) or electromagnetic (e.g., the electromagnetic ion cyclotron wave (EMIC) and the dispersive Alfvén wave (DAW)), broadband or monochromatic — have been observed to associate with these TAIs, and they all are thought to be able to accelerate the O^+ ions perpendicularly, lifting them up in cooperation with the magnetic mirror force (Norqvist et al., 1998). At higher altitudes — up to several earth radii (R_E), electrostatic structures, including the 100-km-scale inverted-V structures, double layers, LH solitary structures, etc., may continue to accelerate the ions that were thrust upward by low-altitude waves (Bostrom, 1992; Schuck et al., 2003; Cui YB et al., 2014). By comparing the energies of O^+ ions at different altitudes below 6 R_E, the higher-altitude perpendicular accelerations are found to be saturated at altitudes of ~4.5 R_E (Bouhram et al., 2004). These O^+ ions then flow up adiabatically along the magnetic flux tube; in the meantime they move tailward with the magnetospheric convection flow. These O^+ ions thus exhibit an altitude-energy dispersion property that is a velocity filter effect in which the higher-energy O^+ ions always tend to lead the lower-energy ions in altitudes within a magnetic flux tube (Horwitz, 1986; Dubouloz

et al., 1998). After reaching the tail plasma sheet, the O+ ions can be ejected earthward (Fu SY et al., 2002); the enhanced convection electric field, its variations, the Betatron and Fermi accelerators, all contribute to further energization during their inward transportation or diffusion, which finally feed these ~keV O+ ions into the ring current and thus enhance the current (Welling et al., 2015). Even inside the ring current, the EMIC waves excited by the anisotropic hydrogen ions (Wang ZQ et al., 2017) or the ULF waves driven by dayside solar-wind perturbations, or by nightside fast flows (Zong QG et al., 2012) can continue the acceleration and thus further intensify geomagnetic storms. The journey of these O+ ions inside the magnetosphere is long; they may take hours to travel from the polar ionosphere, via the polar caps and the magnetotail, and finally to the inner magnetosphere (Lui, 1993).

Hasegawa (1976) proposed the DAW as a candidate mechanism for O+ acceleration/transportation in the context of energy precipitating from the magnetosphere to the ionosphere and of waves cascading from the macroscopic to microscopic scales. Chaston et al. (2016), Chaston et al. (2015b) and Chaston et al. (2014) attributed the perpendicular acceleration of the O+ ions to their resonances with kinetic scale field lines, which occur all along a flux tube, not limited within certain altitudes over the polar ionospheres. The magnetohydrodynamic (MHD) perturbations, driven by the fast reconnection flows from the magnetotail (Chaston et al., 2014, 2015a) or by the surface waves on the magnetopause (Hasegawa, 1976; Chaston et al., 2005, 2007b), are thought to be mode-converted to the DAWs with the perpendicular wave length down to ion-gyroradius (i.e., KAW) or even to electron-inertial scale (inertial Alfvén waves, IAW) (Stasiewicz et al., 2000a). The different power spectral densities (PSDs) of the waves in different plasma regimes supply a good diagnostic tool for the DAWs (Chaston et al., 2015a). In this way, the DAWs have been identified out of the broadband electromagnetic noises in the top ionosphere (Stasiewicz et al., 2000b) as well as in the magnetosphere (Stasiewicz et al., 2000a; Chaston et al., 2007a, 2015b). The parallel electric fields (PEFs) manifest another key characteristic of DAWs (Stasiewicz et al., 2000a). The PEFs cannot only accelerate ions in parallel but can also precipitate aurora electrons that heat the ionosphere below. The buoyant force resulting from the heated electrons may initiate O+ upflows from the ionosphere (Hasegawa, 1976; Chaston et al., 2007a). The DAWs can also accelerate ions perpendicularly and lift their energy quickly to keVs over a time of minutes and over a field-aligned distance of an R_E (Earth radius) (Stasiewicz et al., 2000c; Chen et al., 2001; Chaston et al., 2004). The DAWs have also been observed near the inner plasma sheet boundary (Chaston et al., 2015a, b) or even inside the ring current (Chaston et al., 2015a; Zhang H et al., 2022), where the DAWs are observed repeatedly to accelerate the ring current O+ ions that may have been injected from the downstream tail (Chaston et al., 2014) or have been dragged directly along the closed field lines from the aurora zone, also by the DAWs (Chaston et al., 2016; Gkioulidou et al., 2019; Zhang H et al., 2022). The field-aligned transport in the latter scenario completes in minutes (Zhang H et al., 2022), thus providing a simple but efficient way for the inner magnetosphere to respond quickly to outside perturbations, such as to sudden magnetopause compressions or pounding of nightside reconnection flows (Hasegawa, 1976). Nevertheless, so far, only a few cases have been reported in the literature that support the simple O+ transport picture; the DAWs are not yet widely-

accepted as a mechanism for the heavy ion upflows.

In this paper we show that the large-scale inverted-V upflowing O+ ion channels (IVOCs) have been observed frequently near the open-closed field line boundary over the high-latitude ionospheres at all local times. When the observing satellite traversed these field-aligned structures, the O+ ion energy peaked in the central region of the IVOCs, which characterizes the inverted-V shapes in the time-energy spectra of the upflowing O+ ions.

Three IVOC cases are reported in this paper, representing situations on the dayside (near the equatorial boundary of the cusp/cleft region), on the nightside (near the plasma sheet boundary), and on the flank (near the dawnside open-closed field line boundary), respectively. In these cases, all the IVOCs occurred closely associated with MHD Alfvén waves that were propagated downward and had cascaded down to small-scales to be the DAWs. The DAWs may have accelerated — and/or have still been accelerating — the O+ ions perpendicularly; the two situations are hard to distinguish in the data analyzed in this paper. The upward PEFs of DAWs were observed within the channels, which can precipitate aurora electrons downward, initiating the O+ upflows into the ionosphere (Hasegawa, 1976; Chaston et al., 2007a; Zhang H et al., 2022), or even accelerating the O+ beams upward. Both the perpendicular and parallel accelerations raise the O+ energies more significantly in the central region of the IVOCs, creating the inverted-V structures. Statistics on five-years of C3/Cluster observations show that IVOCs prefer high or highly-fluctuated solar wind dynamic pressures (P_{dyn}) during geomagnetic perturbations. Near the open-closed field line boundary, the stronger the wave power, the higher the field-aligned differential O+ flux and the higher the beam energy, indicating that the DAWs are the accelerator. The frequent presence of large-scale inverted-V structures suggests that the DAWs are of great importance for the transport of heavy ionospheric ions from all around the magnetic poles of the Earth.

2. Instrumentations and Coordinate Systems

From 2001 to 2005, the Cluster satellite constellation flew along polar orbits with apogees and perigees of ~4.4 and ~19.2 R_E, respectively. Every year, the orbits swept clockwise around the Earth's magnetosphere, allowing measurements at all longitudes of the magnetosphere over the polar ionospheres (Escoubet et al., 2001). This work utilises the 4-second-resolution ion and electron data from CIS (Réme et al., 2001) and PEACE (Johnstone et al., 1997) instruments onboard the C3/Cluster. Also used are data from the FGM (0.25 Hz) (Balogh et al., 2001), STAFF (CWF 25 Hz) (Cornilleau-Wehrlin et al., 1997) and EFW (LEFW at 0.25 Hz and EFW at 25 Hz) (Gustafsson et al., 2001) instruments measuring magnetic and electric fields.

Three types of coordinate systems, i.e., the Geocentric Solar Magnetospheric (GSM), the Solar Magnetic (SM), and the Magnetic Field-Aligned (MFA) coordinate systems, are adopted when necessary. In the MFA coordinate system, the $\hat{z}$ axis points along the background geomagnetic field $\boldsymbol{B}$, the azimuthal $\hat{a}$ axis is along $\boldsymbol{r}_{sc} \times \hat{z}$, where $\boldsymbol{r}_{sc}$ is the position vector of the observing satellite C3, and the radial $\hat{r}$ axis completes the right-hand orthogonal set through $\hat{z} \times \hat{a}$. In the polar magnetosphere, $\hat{z}$ typically

points southward and thus $\hat{a}$ is basically eastward.

3. Case Studies

3.1 A Dayside Case

A case on Sep 23rd, 2001, in which the IVOCs occurred in the dayside of the magnetosphere near the equatorial boundary of the cusp/cleft regions over both the south and north magnetic poles, is studied. The OMNI datasets show that, from 07:45 UT to 13:30 UT, the interplanetary magnetic field (IMF) was below 20 nT and dominantly in the -Y and -Z directions in GSM (Panel 1a in Figure 1). Under this condition, magnetopause reconnection may have easily occurred on the magnetopause (Zhang H et al., 2019). The solar wind $P_{\rm dyn}$ was highly fluctuated, and its magnitude was basically larger than 5 nPa, occasionally reaching ~10 nPa, one order higher than normal (Panel 1b). These fluctuations may have excited magnetopause surface waves (Archer et al., 2019). The *Dst* index remained small, and the perturbations in the *AE* index reached a level over 600 nT (Panel 1c), suggesting intense substorm-like activity inside the magnetosphere.

During this period, C3/Cluster moved northward near the noon meridian via its perigee in the dayside magnetosphere (Panels 1r and 1s). In the polar regions (before 08:57 UT or after 11:42 UT), both the magnetic field (Panel 1d) and the densities of different species (Panel 1e) were highly fluctuated. The parallel, antiparallel and omni O^+ energy-spectra in Panels 1f–1h show some special patterns in high latitudes: multiple upward O^+ beams occurred in both hemispheres (the parallel beams in the south hemisphere in Panel 1f and the antiparallel in the north in Panel 1g, embraced by the two pair of white vertical lines, respectively); the beam energies reached ~1 keV at the centers of the structures forming large-scale inverted-V structures (the red/yellow structures in Panels f and g) . There were the higher-energy tails in the energy spectra extending up to ~5–10 keV at the centers (the higher-energy electrons above the red inverted-V structures in Panels f and g). Hereafter in the paper, these structures are referred to as the IVOCs.

Three major IVOCs appear in this case, two in the south hemisphere (referred to as S-IVOCs; the period of these two IVOCs is embraced by the first pair of white vertical lines in Figure 1, the two S-IVOCs appearing before and after 08:42 UT, respectively) and one in the north (N-IVOC, embraced by the second pair of vertical lines in Figure 1). The geomagnetic field lines modelled by using the Tsyganenko model (T05) (Tsyganenko and Sitnov, 2005) are plotted in Panels 1r and 1s. The trajectory of C3/Cluster from 07:45 to 13:30 UT is projected to the X-Z and Y-Z planes of the GSM coordinate system in Panels 1r and 1s, respectively. The portions of the trajectory through the S-IVOCs and N-IVOC with the periods corresponding to the two pairs of the vertical lines in the left panels are marked in red, showing that these IVOCs are of scales of ~$R_{\rm E}$ across field lines or of latitudinal width of ~10° in magnetic latitudes (MLats) (Panel 1r). The IVOCs are obviously not of the microscale of 100-km inverted-V channels previously reported (Cui YB et al., 2014). The two blue (green) modelled field lines are plotted in Panel 1r denoting the equatorial and polar boundaries of the S-IVOCs (N-IVOC), respectively. It is seen that the field lines in the most poleward portion of the IVOCs are open while the

lines in the most equatorial portion are closed. To identify the connectivity of the field lines, the pitch angle (PA) spectrum of 10 eV–30 keV electrons is also adopted (Panel 1q). Considering their thermal velocities over 10^4 km/s, these electrons should have been quickly emptied onto open field lines while been trapped on closed fields. In this sense, the two S-IVOCs may occur on the closed field lines (equatorward of the southern cusp/cleft) since the keV electrons do exist; the small portion of the field lines inside the N-IVOC are closed but the rest are open because the keV electrons appear only briefly but disappear through the greater portion of the N-IVOC (inside the northern cusp/cleft). These observations suggest that the IVOCs form near the cusp regions (open field lines) but are not necessarily limited to within the cusps/clefts. In other words, the O^+ ions flew upward near the open-close field line boundary in the dayside polar magnetosphere. In fact, the IVOC structures in the cusp/cleft are not a new thing, having been reported, also inside the northern cusp/cleft Bouhram et al. (2004) in an IVOC event very similar to the N-IVOC in this event.

Both the magnetic and electric waves burst in the center of the IVOCs. The low-frequency magnetic disturbances are already visible in Panel 1d. By subtracting 400-second sliding-window-averaged backgrounds $B_{\rm bg}$, the magnetic perturbations, d$B = B − B_{\rm bg}$, in Panel 1k show clearly that the low-frequency perturbations occur mainly in the two perpendicular components, dB_a (blue in Panel 1k) and dB_r (green), but not significantly in the parallel component, dB_z (red), which indicates low-frequency MHD Alfvén waves. The PSD of dB_r measured by the STAFF and FGM instruments, are displayed in Panels 1i and 1j, respectively. The low-frequency Alfvénic perturbations (Panel 1j) inside the IVOCs, especially at the center, are seen clearly to extend into the high-frequency band (Panel 1i). The electric waves, dE_a, observed by the EFW in the orthogonal direction of dB_r, also burst within the low-frequency (Panel 1m) and high-frequency (Panel 1l) bands, closely associated with the broadband magnetic waves.

Spectral analyses similar to what Chaston et al. (2015a) have done are performed to diagnose DAWs. The black bars on the top of Panels 1k and 1n mark the periods of the data involved. The PSDs of dB_r and dE_a are plotted by dots as functions of the observed frequency $f_{\rm SC}$ in Panels 1t and 1u, respectively; the black curves plot the average PSDs within a set of logarithmically-spaced frequency bins. Both the PSDs decrease as $f_{\rm SC}$ increases. The averaged PSD of dB_r follows power laws, $PSD = Af_{\rm SC}^{-\beta}$. β remains constant at 2.3 below, and 3.6 above the break that occurs at $f_b = 0.4$ Hz (the green lines in Panel 1t). These linear PSDs represent DAWs, and the break frequency may indicate the mode conversion between different plasma regimes (Chaston et al., 2014, 2015a). The phase velocity, $V_P = {\rm d}E_a/{\rm d}B_r$, is plotted in Panel 1v as a function of frequency. V_P remains below 10^6 m/s when the frequency is <0.01 Hz, a typical quantity of MHD Alfvén velocity in the magnetosphere. V_P rises as $f_{\rm SC}$ increases, reaching $10^7–10^8$ m/s beyond f_b. It is seen that the phase velocity varies when the frequency changes, and that's why these waves are named DAWs.

PEFs are the other key feature of the DAWs (Stasiewicz et al., 2000a). Notice that only two orthogonal components of *E* within the spin plane of C3/Cluster are measured correctly; because of
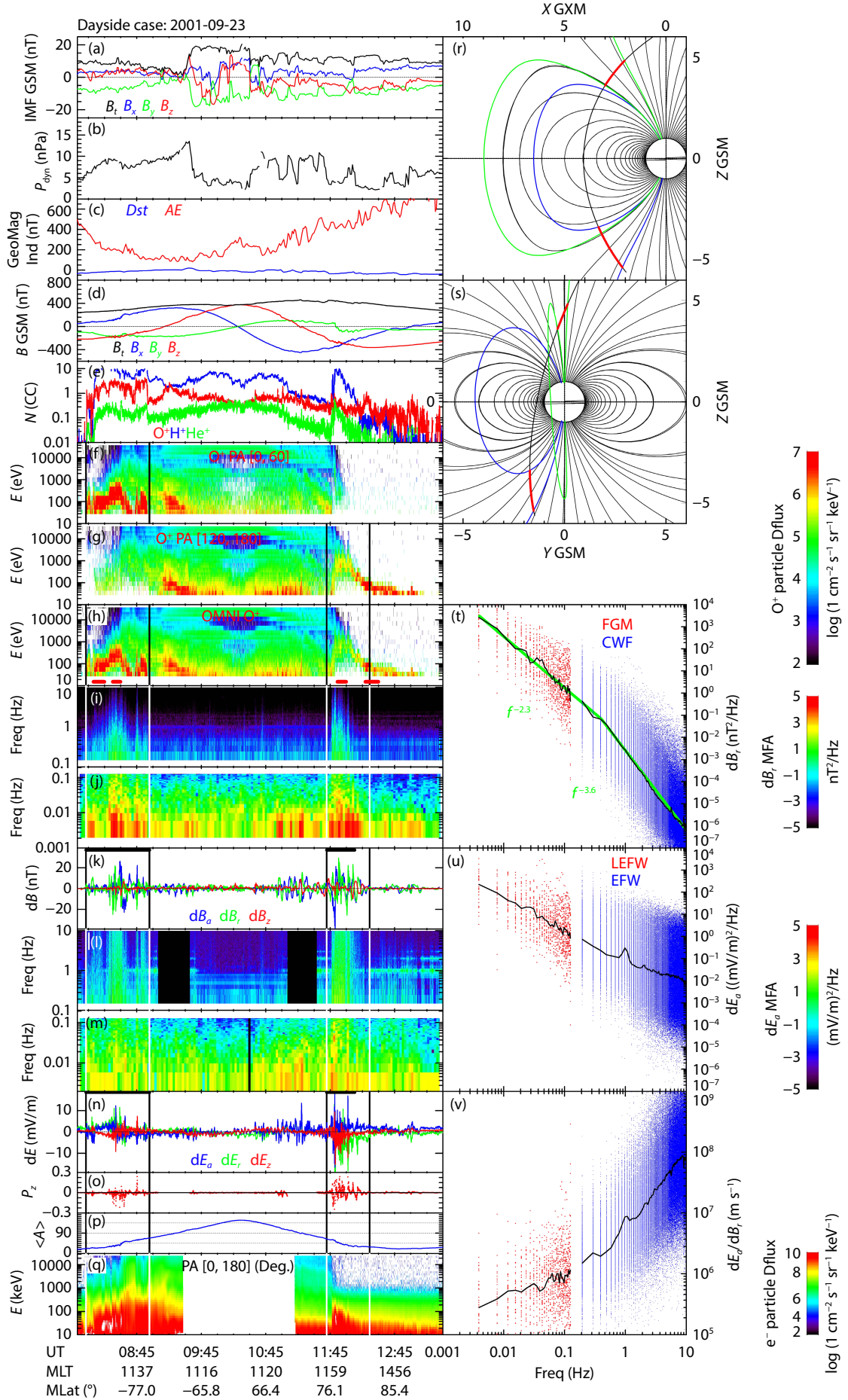
Zhang H et al.: Large-scale inverted-V O⁺ channels

Figure 1. The dayside case of IVOCs on Sep 23rd, 2001. (a) the three components and magnitude of the IMF in the GSM coordinate system; (b) the solar wind dynamic pressrue P_{dyn}; (c) the *AE* and *Dst* indices. (d–v) show the C3/Cluster observations, and (d) the three components and magnitude of magnetic field in the GSM coordinate system, (e) the ion densities of the hydrogen (H$^+$, blue), oxygen (O$^+$, red) and nitrogen (He$^+$, green) species, (f–h) the parallel, antiparallel and omni O$^+$ ion differential fluxes, (i–j) the PSDs of dB_r of the high frequencies (i, >0.1 Hz) from the STAFF instrument and of the low frequencies (j, <0.1 Hz) from the FGM instrument, (k) the three components of d$\boldsymbol{B}$ relative to the 400-second sliding-window-averaged FGM data, (l–m) the PSDs of dE_a of the high frequencies (l, >0.1 Hz) and of the low frequencies (m, <0.1 Hz) both from the EFW instrument, (n) the three components of the 4-second resolution d$\boldsymbol{E}$, (o) the field-aligned Poynting fluxes P_Z, (p) the cross-angles ⟨A⟩ between the background magnetic field and the satellite spin axis, (q) the PADs of 1–30 KeV electrons, (r–s) C3/Cluster's trajectory projected to the *X-Z* (r) and *Y-Z* (s) planes in the GSM coordinate system (the red trajectories denote the corresponding periods of the IVOCs, and the other curves are the modelled field lines), and (t–v) the PSD spectra of dB_r (t), dE_a (u) and dE_a/dB_r (v) (the data involved these spectrum analyses are marked by the black bars in Panels (k) and (n) in this figure). The two pairs of white vertical lines embrace the two groups of the IVOCs in the south and north hemisphere, respectively. The vector parameters in Panels (k), (n) and (o) are plotted in the MFA coordinate system, and in GSM coordinate system in the other panels. Dflux = differential flux.

calibration problems, the component along the spin axis $\hat{s}$ is not. Therefore, when $\boldsymbol{B}$ is perpendicular to $\hat{s}$, the PEF E_Z and one of the perpendicular components can be measured correctly; when $\boldsymbol{B}$ is parallel/anti-parallel to $\hat{s}$, the two perpendicular components E_a and E_r can be obtained while E_Z cannot. Panel 1p displays the cross angles ⟨A⟩ = ⟨$\hat{s}, B$⟩ between the satellite's spin axis and the instantaneous background magnetic fields. Panel 1n shows the three components of $\boldsymbol{E}$ measured within the spin plane in the MFA coordinate system; the red curve indicates the presence of the PEF E_Z inside the IVOCs. E_Z is positive (negative) associated with the strong waves in the center of the S-IVOCs (N-IVOC) when ⟨A⟩ ~ 45°. Within the IVOCs, the cross angles ⟨A⟩ are not 90° but near 45°, under which condition the PEFs E_Z are not measured completely. The polarity of E_Z is basically positive in the south hemisphere while negative in the north, both upward, which may indicate the presence of upward PEFs. These upward PEFs are thought to be able to precipitate aurora electrons, initiate iono-spheric O$^+$ upflows, and accelerate/lift the ions (Chaston et al., 2007a).

The field-aligned Poynting flux is estimated through $P_Z =$ (d$\boldsymbol{E}_{a,r} \times$ d$\boldsymbol{B}_{a,r}$)$/\mu_0$ in Panel 1o in the MFA coordinate system. P_Z fluctuates highly but mainly in the $-\hat{z}$ ($+\hat{z}$ or downward direction inside the S-IVOCs (N-IVOC) when ⟨A⟩ > 45°. The P_Z periodically peaks and the peaks may represent the real parallel Poynting fluxes, because the perpendicular components d$\boldsymbol{E}_{a,r}$ of d$\boldsymbol{E}$ can be measured correctly when it rotates to near the satellite spin plane. These downward Poynting fluxes describe a scenario in which energy sources are located in the outer magnetosphere, probably driven by surface waves on the dayside magnetopause because of the highly-fluctuated solar wind dynamic pressure P_{dyn} in this case (Panel 1b), and the energy is carried by the MHD Alfvén waves to precipitate into the polar ionosphere (it will be seen later that a portion of the energy may have been transferred to the precipitating electrons).

Figure 2 adopts the pitch angle distributions (PAD) for O$^+$ ions and electrons inside the IVOCs to examine acceleration. The left plots show the O$^+$ ion PADs, and the right panels show the ratios of electron fluxes at pitch angle (θ) to that at the conjugated angle (180°−θ) which characterizes the isotropy level of the electron distribution. Panels 2a and 2b (2c and 2d) present the data in the central and edge regions of the S-IVOC (N-IVOC), respectively; the time periods of the data are labeled by the red bars at the bottom

of Panel 1h in Figure 1. In the central regions, where the DAWs are strong, the O$^+$ PADs expand in the perpendicular directions (the oblique O$^+$ ions are of energies greater than those of the parallel (antiparallel) ions in the left plots of Panel 2a (Panel 2c)). This is the second type of TAIs as discussed by Bouhram et al. (2004). Particularly, the N-IVOC in this event is very similar to the case reported by Bouhram et al. (2004) in which they have attributed the inverted-V structure to the local acceleration by broadband extremely low frequency waves in the center of the structure. In this case, the perpendicular acceleration can be performed also by the broadband low frequency waves in the central IVOCs that have turned out to be the DAWs. The O$^+$ ions observed at the IVOCs' edge are adiabatic because they have the partial ring-like PADs (the oblique and parallel/antiparallel O$^+$ ions are of the same energies, in the left plots of Panels 2b and 2d); there is no strong DAW associated with these ions and thus no significant accelera-tion. Comparing the ion PADs in Panels 2a and 2b or in Panels 2c and 2d, it is seen that the O$^+$ ion energies in the center of the IVOCs are not only higher in the oblique directions but also higher in the parallel/antiparallel directions than those adiabatic O$^+$ ions at the edge regions; the parallel/antiparallel acceleration in the center of the IVOCs may arise from either pitch angle folding (because of the mirror force after being accelerated perpendicu-larly) or parallel acceleration by the upward PEF (Klumpar et al., 1984). Besides accelerating the ions, the PEFs may also accelerate and precipitate electrons downward to the polar ionosphere. In the right plots of Panels 2a and 2b for the S-IVOCs, the electron fluxes on closed field lines are slightly but systematically higher in the antiparallel direction, indicating downward precipitation. The field lines inside the N-IVOC are mainly open. The low-energy (< 1 keV) electrons are present and flowing upward (antiparallel to magnetic field lines in the north hemisphere, in the right plots of Panels 2c and 2d) together with the O$^+$ ions. These low-energy electrons could be those ionospheric electrons heated by the high-energy electrons precipitated from the magnetosphere (Hasegawa, 1976; Chaston et al., 2007a; Zhang H et al., 2022). The high-energy (> 1 keV) electrons are of the very low differential fluxes because of the open field lines (Panel 1q in Figure 1), but these electrons are seen to be precipitating (the parallel > 1 keV electrons in the right plots of Panel 2c and 2d) just as observed on the closed field lines in the southern hemisphere (the antiparallel >1 keV electrons in the right plots of Panels 2a and 2b). Through the PEFs, a portion of energy may have been transformed from
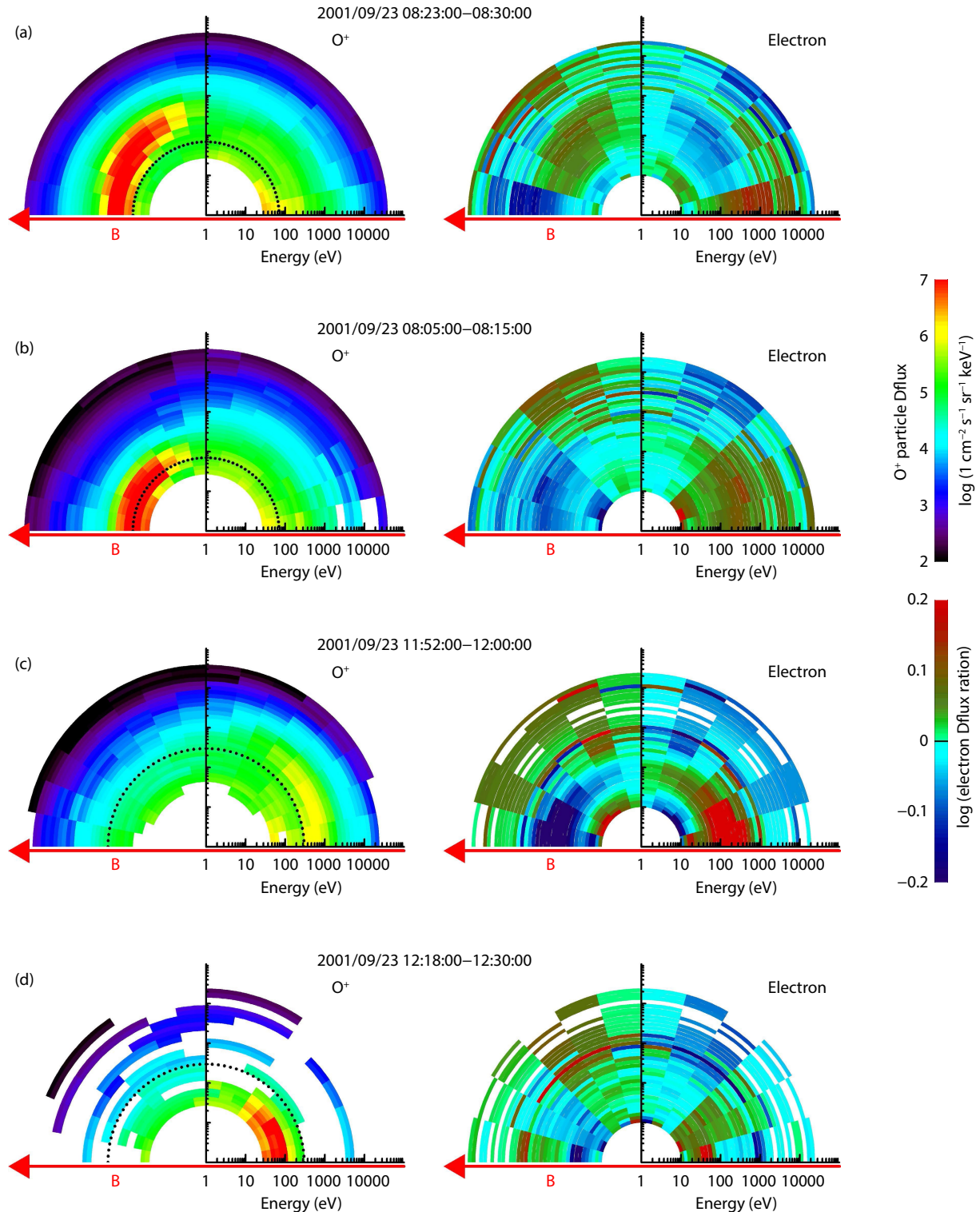
Figure 2. The PADs of O+ ions (left) and the PADs of the differential flux ratios of the electrons of the conjugate pitch angles (right). Panels (a–b) and Panels (c–d) are the data inside the south and north hemispheric IVOCs, respectively. Panels (a) and (c) are in the center of the IVOCs, whereas Panels (b) and (d) are at the edge. The red bars in Panel 1h of Figure 1 mark the data periods adopted in Figure 2.

the DAWs to the keV electrons.

3.2 A Nightside Case

A nightside case of IVOCs occurred on Feb 14, 2003, observed by C3/Cluster when the satellite was moving northward via its perigee from 12:30 UT to 16:00 UT (Figure 3). Zhang H et al. (2022) have reported a nightside event of O+ ion upflows driven by DAWs near the magnetic equator; the case studied here, however, occurred over the polar ionospheres, far away from the equator. The OMNI datasets show that during this period the solar wind dynamic pressure P_{dyn} remained 3 nPa (Panel 3b), quite stable
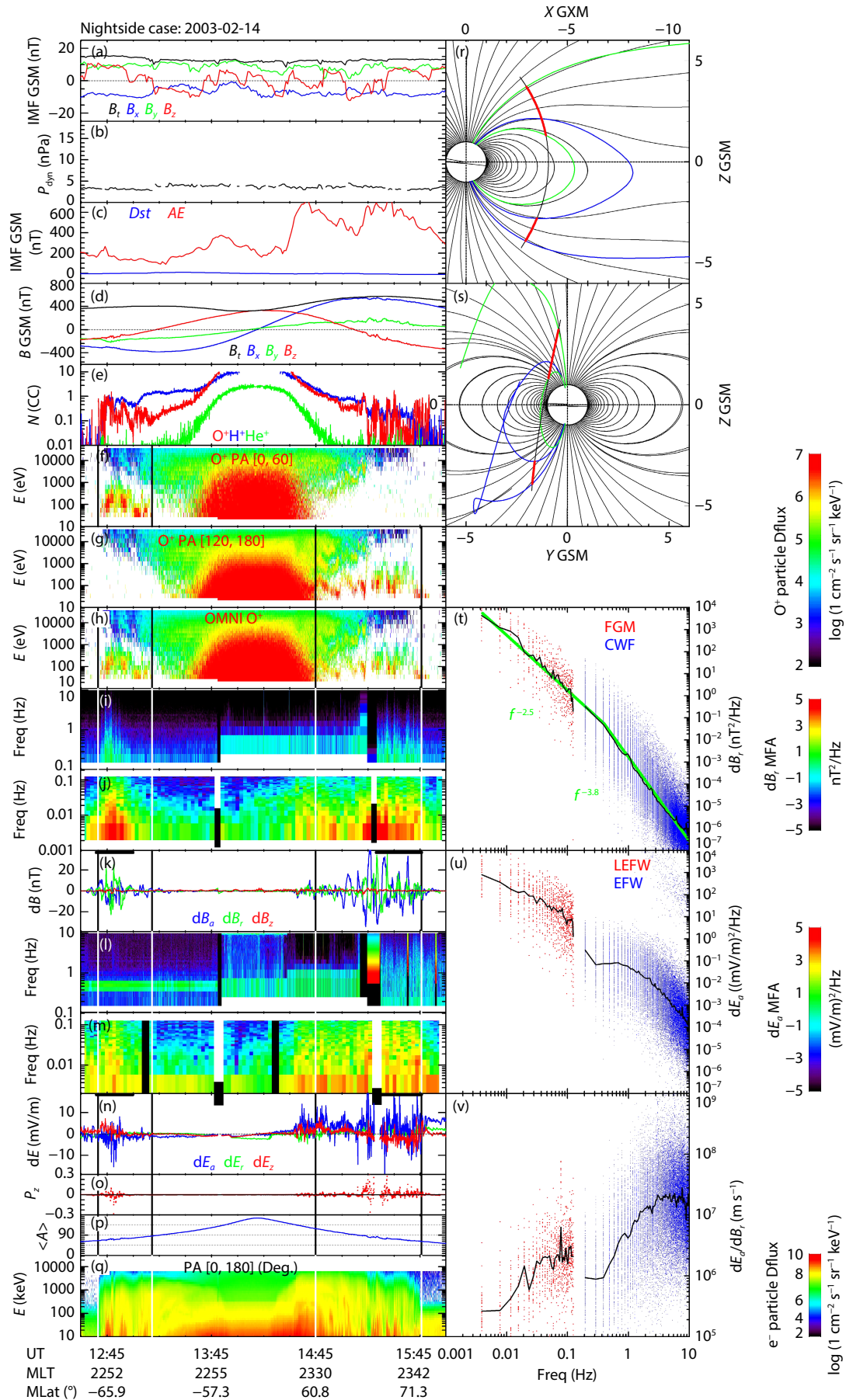
Figure 3. The nightside case of IVOCs on Feb 14, 2003. The formats of this figure are the same as those of Figure 1.

Zhang H et al.: Large-scale inverted-V O⁺ channels

compared with the dayside case in Figure 1. The B_Y component dominated the IMF in GSM, and B_Z was basically southward but occasionally turned northward (Panel 3a in Figure 3), in which situation the *AE* index increased step by step as seen in Panel 3c; the substorm-like geomagnetic perturbations also strengthened step by step. The variations of the magnetic field (Panel 3d) and the ion densities (Panel 3e) indicate that the observing C3/Cluster traversed the near-Earth plasma sheet from south to north; these data are consistent with the satellite trajectory shown in Panel 3r (*X*-*Z* plane) and Panel 3s (*Y*-*Z* plane).

After the satellite entered the plasma sheet from the south lobe region and before the satellite left the plasma sheet into the north tail lobe, i.e., inside the two plasma sheet boundary layers, two groups of IVOCs were encountered, respectively. In the south hemisphere, the O^+ ions were moving along the magnetic fields (between the first two pair of white vertical lines in Panel 3f), while in the north hemisphere, the O^+ ions were against the field lines (between the second two pair of white vertical lines in Panel 3g). The beam energies of the upflowing O^+ ions peaked for multiple times in both hemispheres, forming the multiple IVOCs; the largest differential O^+ ion fluxes occur typically beside the energy peaks (Panels 3f–3h). The high-energy electrons (1–30 keV) showed up clearly from 12:40 UT to 15:45 UT (Panel 3q), indicating the closed field lines inside the plasma sheet. Although the two groups of IVOCs are seen to be located on the closed field lines in the tail, unlike the equator case reported by Zhang H et al. (2022), no counter-streaming O^+ ions are observed at the low altitudes in this event.

The IVOCs in this case are all associated with bursts of broadband electric and magnetic waves. Panel 3k shows the three components of the magnetic field perturbations $d\boldsymbol{B} = \boldsymbol{B} - \boldsymbol{B}_{bg}$ in the MFA coordinate system, where $\boldsymbol{B}$ is the observed magnetic field and $\boldsymbol{B}_{bg}$ is the 400-second sliding-window-averaged background. It is clearly seen that the low-frequency perturbations occurred closely associated with the IVOCs (the periods are embraced by the two pairs of vertical lines). These magnetic perturbations are only in the two perpendicular orthogonal components, dB_a and dB_r, but not in the field-aligned component, dB_Z, indicating that these low-frequency perturbations are Alfvénic. These low-frequency magnetic perturbations are also seen in the PSD of the dB_r component in Panel 3j, and in Panel 3i are seen to extend into the high-frequency band (although some high-frequency data are not good). All these magnetic perturbations are accompanied by electric field perturbations in either low-frequency or high-frequency bands in the orthogonal component, dE_a, as seen in Panels 3l and 3m. The spectral analyses of both dB_r and dE_a (Panels 3u–3v) indicate that these broadband fluctuations are DAWs; again, a break in the mode conversion frequency occurs near $f_b = 0.4$ Hz (the green lines in Panel 3t). Although the magnitude of the high-frequency electric field perturbations from the EFW instrument may have been underestimated (Panel 3u), the phase velocities, $V_P = dE_a/dB_r$, in Panel 3v still show that V_P in the low-frequency band is 10^5–10^6 m/s, a typical quantity in the MHD regime, and V_P increases to ~10^7 m/s at the high-frequency end, indicating that the broadband fluctuations are characteristic of DAWs (Chaston et al., 2015a).

The most valuable feature of this case is the PEF E_Z and the parallel Poynting flux $P_Z = (d\boldsymbol{E}_{a,r} \times d\boldsymbol{B}_{a,r})/\mu_0$. During the two groups of the

IVOCs, the cross-angle $\langle A \rangle = \langle \hat{s}, \boldsymbol{B} \rangle$ remains close to 90° (Panel 3p), which means that, as analyzed in the dayside case, the PEF E_Z can be measured correctly. The red curve in Panel 3n show that E_Z remains positive (negative) inside the IVOCs in the south (north) hemisphere, indicating that the PEFs point upward along (against) the field lines. P_Z peaks periodically and the peak quantities well represent the real parallel Poynting flux when $d\boldsymbol{E}_{a,r}$ rotates to within the satellite's spin plane. The Poynting flux P_Z, however, has polarities opposite to E_Z, and P_Z is negative (positive) (Panel 3o) in the south (north) hemisphere, indicating that the electromagnetic energy is precipitating into the polar ionosphere regions, carried by the Alfvénic waves. The downstream magnetotail can be the energy source for these electromagnetic fluctuations. Throughout this case, the substorm-like geomagnetic perturbations are always presents (Panel 3c). The high-speed flows from the mid-tail of the magnetosphere may excite the Alfvénic waves in the near-Earth flow braking region, which propagate downward along field lines and cascade down to the DAWs, as observed. The scenario is the same as the nightside event reported by Zhang H et al. (2022). In that event, the DAWs were observed to repeatedly accelerate the bouncing O^+ ions near the nightside magnetic equator. In this event, however, the DAWs were observed to accelerate O^+ ions only upward to form the IVOCs in the magnetic field line converging regions at the lower altitudes over the polar ionosphere regions.

3.3 A Dawnside Case

A third case of IVOCs occurred on Dec 3rd, 2001, also closely-associated with the DAWs but on the dawnside of the magnetosphere. In this case, two groups of IVOCs (two in the south hemisphere and two in the north, Panels 4f–4h, embraced by the two pairs of vertical white lines) were encountered by C3/Cluster when this satellite traversed the dawnside magnetosphere northward via its perigee (Panels 4r and 4s). The IVOCs, particularly the central regions, are all accompanied by bursts of broadband electromagnetic waves (waves in dB_r in Panels 4i–4k, and in dE_a in Panels 4l–4n). The low-frequency magnetic field data show that the waves are Alfvénic because the magnetic perturbations occur only in the two perpendicular components, dB_r and dB_a (Panel 4k); the wave spectrum analyses in Panels 4t–4v indicate that these waves are DAWs according to Chaston et al. (2015a). The OMNI datasets in Panels 4a–4c show that the solar wind dynamic pressure P_{dyn} remains almost constant at 2 nPa, and that the IMF was basically dawnward and southward during the IVOCs. Under this IMF condition, the substorm may occur inside the magnetosphere and the associated high-speed earthward flows from the magnetotail may drive the Alfvénic perturbations in the near-Earth region, as observed.

Besides the IVOCs, there are field-aligned upflowing O^+ ions on the higher latitudes in the south cusp region (before 17:53 UT in Figure 4). Although they exhibit in the form as O^+ ion beams or even as IVOCs, there is basically no DAW, indicating that these upflowing O^+ ions may have been accelerated before encountering the observing satellite and that now they are just moving upward adiabatically, as suggested by Bouhram et al. (2004), whose statistical analysis found that the beam energy of O^+ ions saturates at
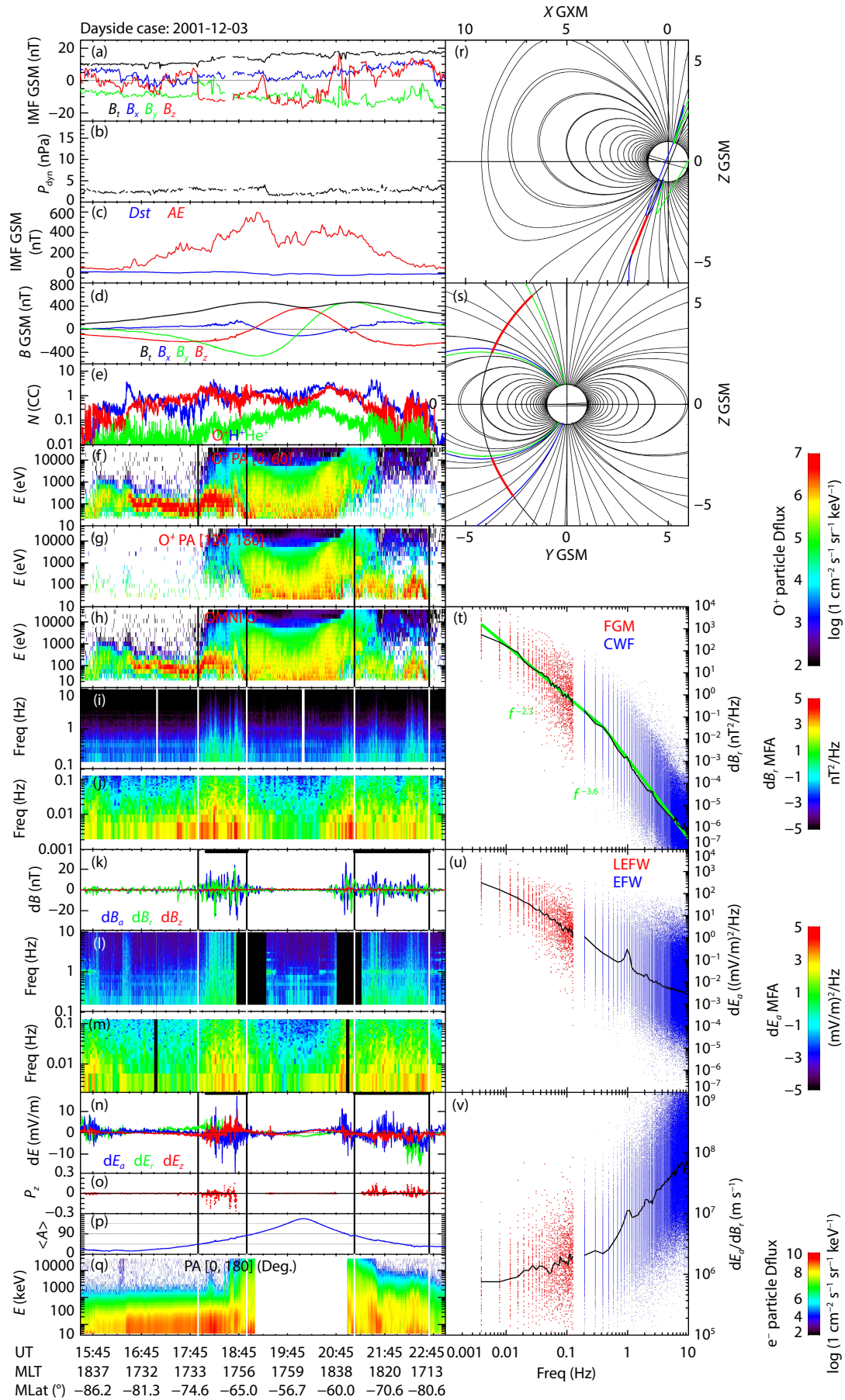
Figure 4. The dawnside case of IVOCs on Dec 3rd, 2001. The formats of this figure are the same as those of Figure 1.

**Zhang H et al.: Large-scale inverted-V O⁺ channels**

altitudes beyond 4.5 R_E, from which they concluded that the accelerator may be located inside the lower-altitude polar cusp/cleft that is upstream (sunward) of the observing satellite.

The PEFs and the parallel Poynting flux are still the key quantities to diagnose the DAWs and their energy source. Although the cross-angle $\langle A \rangle = \langle \hat{s}, \boldsymbol{B} \rangle$ between the background magnetic field $\boldsymbol{B}$ and the spin axis $\hat{s}$ of the satellite C3/Cluster is basically smaller than 90° through the IVOCs (Panel 4p), which is not a good condition to measure the PEFs, the data in Panel 4n show that E_Z values are basically positive inside the south IVOCs (particularly when $\langle A \rangle$ is close to 90°) and negative in the north hemisphere. The systematic change in the polarity of E_Z indicates the presence of real PEFs. The parallel Poynting flux $P_Z = (\mathrm{d}\boldsymbol{E}_{a,r} \times \mathrm{d}\boldsymbol{B}_{a,r}) / \mu_0$ in Panel 4o show that the electromagnetic energy also comes down along the magnetic field lines. The magnetic field lines inside the IVOCs of this case are mainly open in the dawnside boundaries of the polar caps, still near the open-closed field line boundary (Panel 4q).
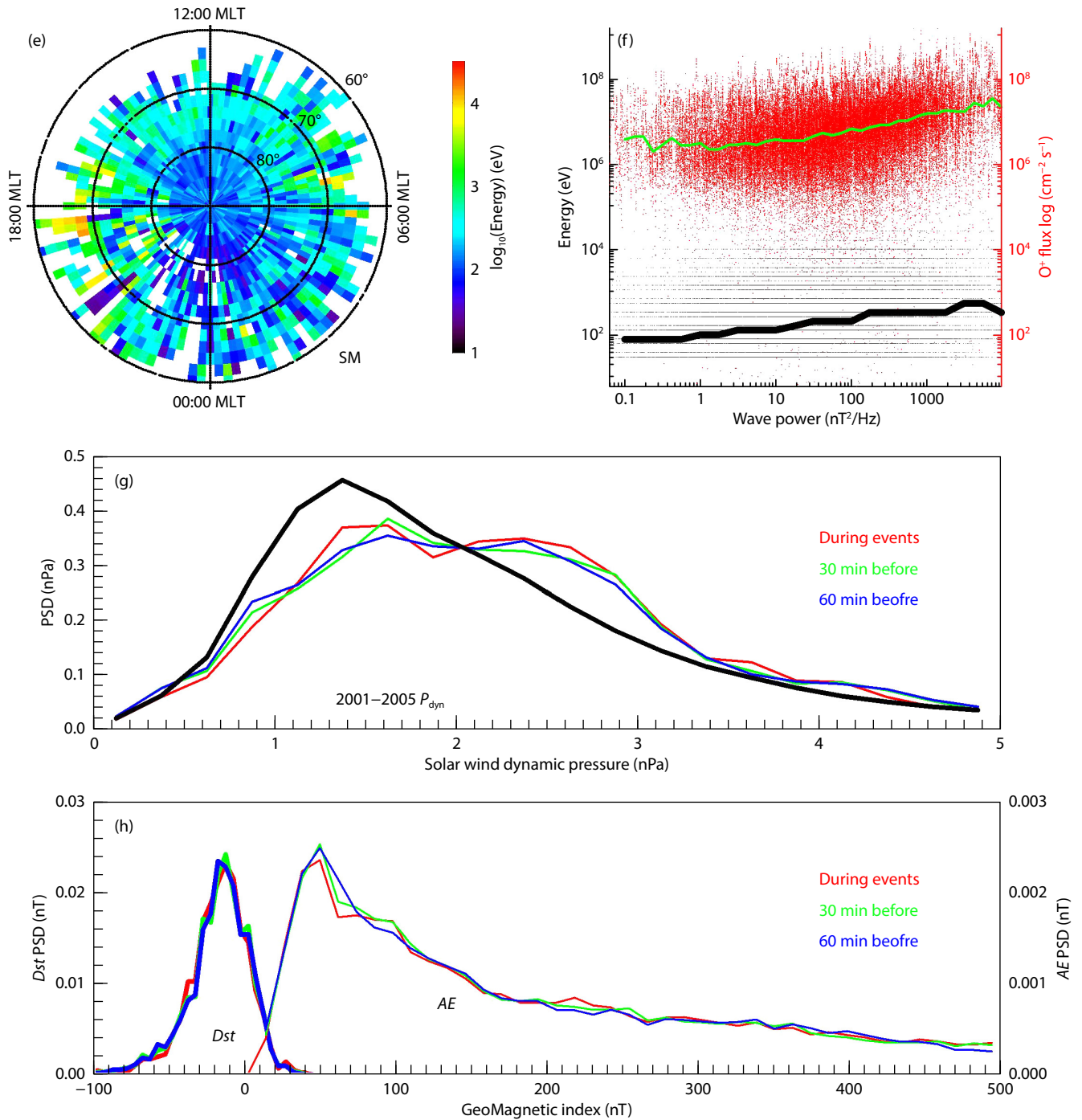
4. Statistics

Based on the energy-spectrum data collected by C3/Cluster from 2001 to 2005, 1790 IVOCs are identified over the polar ionosphere. The magnetic footprints of all the datapoints inside the IVOCs, estimated by using Tsyganenko's T05 model, are distributed as a function of the absolute magnetic latitudes (MLats) and magnetic longitudes (MLons) in Panel 5a in Figure 5. All the cases are seen to fall into the polar ionospheres above 60° in MLats, but the dayside cases are located to the higher latitudes (above 70°). These events are of large-scale; their latitudinal widths range from several degrees to ten degrees, corresponding to ~R_E scales in the magnetosphere (for example, as seen in Panels r and s in Figures 1, 3 and 4). The footprints of datapoints in each event line up basically latitudinally; therefore the longitudinal widths of the IVOCs cannot be estimated in this study. The color code in Panel 5a denotes the field-aligned distance from satellite to ground; the higher-latitude IVOCs are located at the larger altitudes (~9 R_E), a bias that comes from the distribution of the satellite orbits. The upward total O⁺ flux, f_{up}, at each datapoint has been normalized by using the ratio of the magnetic field strengths at C3/Cluster (B_{C3}) and at its magnetic footprint (B_I) $f_N = f_{up}B_I/B_{C3}$. The distribution of f_N in Panel 5b systematically shows the larger f_N on the dayside, indicating that the solar radiation or the ionospheric property is a non-neglectable factor. The dayside f_N reaches 10^7–10^8 /cm²/s statistically, and this dayside O⁺ transport efficiency is commonly as high as those during the extreme nightside case, as reported by Zhang H et al. (2022). A significant O⁺ escape may occur there on the open field lines in the cusp/cleft regions.

Zhang H et al.: Large-scale inverted-V O⁺ channels
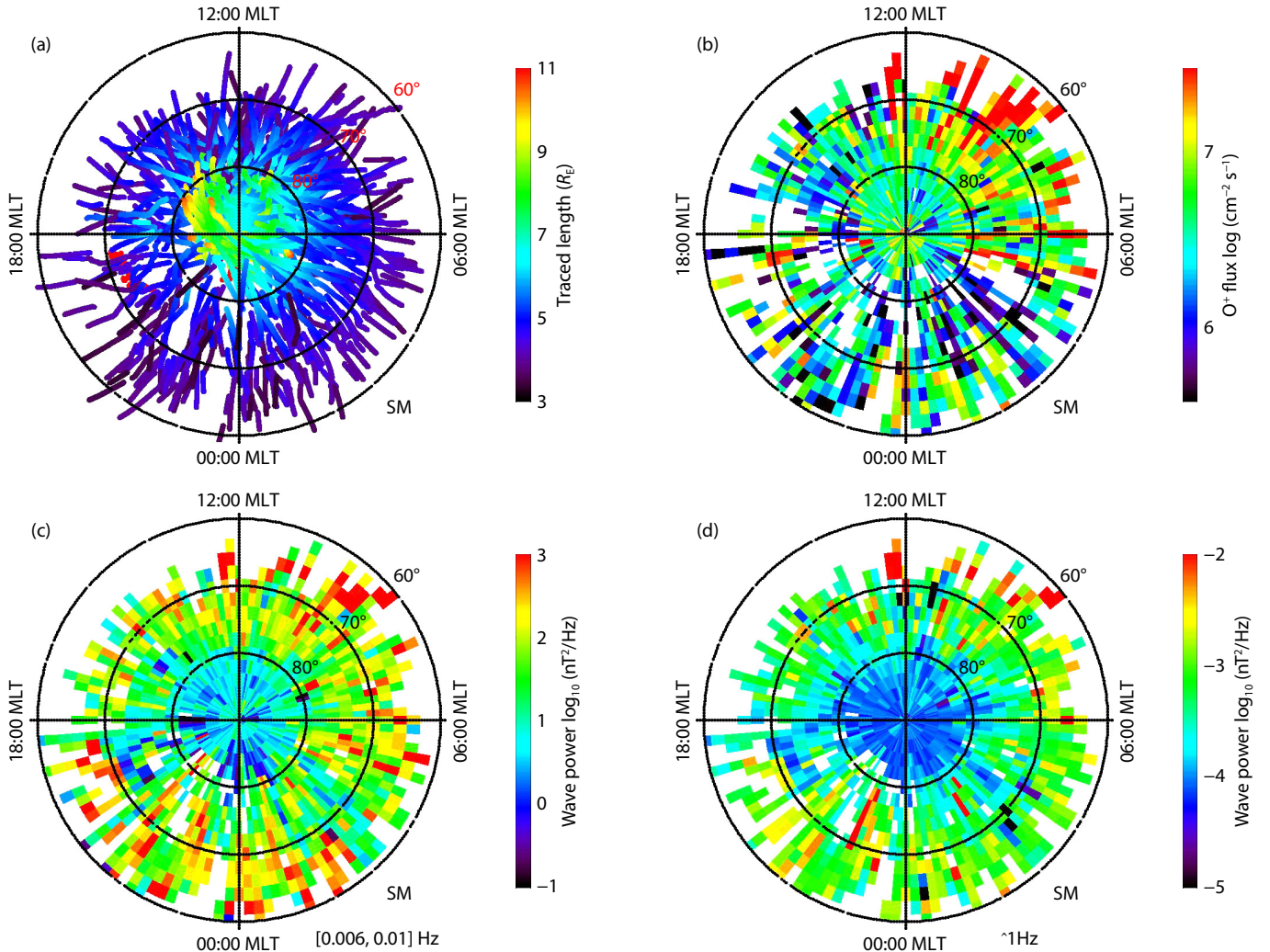
Figure 5. Statistics on the IVOC properties and the external conditions. They are distributions in the SM coordinate system of (a) the magnetic footprints of all the datapoints inside the IVOCs, (b) the normalized upflowing O+ flux f_N, the PSDs of dB_r below 0.01 Hz (c) and at ~1 Hz (d), and the beam energies (e). (f) The beam energies (black dots) and the normalized upflowing O+ flux f_N (red dots) of all the datapoints inside the IVOCs with MLats below 80°, distributed as functions of the PSDs of the 0.008 Hz dB_r; the black and green curves show the bin-averaged quantities of these two parameters. (g) The probability distributions of the solar wind dynamic pressure, P_{dyn}, during the IVOCs (red), 0–30 minutes before (green) and 30–60 minutes before (blue) the IVOCs and during (black) the whole time period from 2001 to 2005. (h) The probability distributions of AE and Dst indices, the color codes are the same as in Panel (g).

The PSDs for dB_r at 0.006–0.01 Hz (MHD regime) and at ~1 Hz (kinetic regime) are distributed in Panels 5c and 5d of Figure 5, respectively. The waves in both regimes are strong below 80° in MLats, where the field lines may connect to the magnetosphere near the open-closed field line boundary. The beam energies for all the datapoints are distributed in Panel 5e; note that they, too, are strong in MLats below 80°, coincident with the strong waves (Panels 5c and 5d). Panel 5f presents correlation analyses of the

beam energies (black dots, Panel 5f) and the normalized O$^+$ fluxes f_N (red dots, Panel 5f) of all the datapoints below 80° in MLats to the wave PSDs at 0.008 Hz. The results show that the stronger the waves, the higher the beam energies (black curve) and the larger the upward O$^+$ fluxes (green curve). No strong waves are observed beyond 80° (Panels 5c and 5d); similarly, the beam energies there are low (Panel 5e), which can reflect a velocity filter effect that, in the cap behind the cusp/cleft, leaves only the lower-energy O$^+$ ions (the higher-energy ions being located at the larger heights), even at the heights larger than those in the lower-altitude acceleration region (Panel 5a).

The external conditions associated with the IVOCs show that the IVOCs occur when the magnetosphere is disturbed. Panel 5g shows the probability distributions of the solar wind P_{dyn} during the events (the red curve in Panel 5g), as well as 30 minutes before (the green curve) and 60 minutes before the beginning times of the events (the blue curve), and during the whole period from 2001 to 2005 (the black curve). Comparison of these distributions shows that P_{dyn} for the IVOCs are overall higher (~2 nPa) and more fluctuated than the normal condition (~1.4 nPa). The probability distributions of the geomagnetic field indices, Dst and AE, during the IVOC events, and 30 minutes and 60 minutes before the events (Panel 5h), indicate that the IVOC events are correlated with global perturbations of the magnetosphere.

5. Discussion

The DAWs have been previously observed at all altitudes, from the ionosphere to the magnetosphere. They occur frequently in the top ionosphere, at altitudes from 600–4200 km, all around the poles with MLats from 60° to 80°; they appear 10° higher in MLats on dayside than on nightside (Stasiewicz et al., 2000a; Chaston et al., 2007a). They are also observed very often in the inner magnetosphere ($L > 3$) near the magnetic equator (Chaston et al., 2015a). In this study, DAWS are found also to occur frequently at altitudes of 4–6 R_E, located in the middle of the polar ionosphere regions and the magnetic equator (Panels 5a, 5c and 5d in Figure 5). The footprints of all these cases are located in Mlats, mainly between 60° and 80° (Panels 5c–5d in Figure 5), in a pattern almost identical to the low-altitude FAST observations (Chaston et al., 2007a). In the equatorial region of the magnetosphere, these waves are observed mainly on the nightside (Chaston et al., 2015a), whereas Zhang H et al. (2022) showed that nightside DAWs occur in fact beside, but not right on, the equator. On the dayside, DAWs are observed to occur less frequently near the equator (Chaston et al., 2015a) but always present in the cusp/cleft regions (Stasiewicz et al., 2000a).

The DAWs provide a simple but efficient and global way to pump the heavy ions, as shown in Figure 6. Chaston et al. (2014) and Chaston et al. (2015a) demonstrated that the filament field line resonances of DAWs are present all the way along a magnetic flux tube between the opposite polar ionosphere regions. They found that DAWs and the associated Poynting flux propagate downward to the ionosphere (Chaston et al., 2005), just as observed in this study. The downward transport of energy, however, is not carried only by the Poynting flux of the waves but also by the precipitating keV electrons, and the energy of the electrons may also result

from the DAWs through the PEF acceleration. It is hard to distinguish which form dominates the precipitating energy (Brambles et al., 2011; Strangeway et al., 2005; Zhao K et al., 2020); the balance may depend either on altitude, since the DAWs keep providing energy to the precipitating electrons as they propagate towards the ionosphere, or depend on magnetic connectivity, since on the open field lines the differential flux of the precipitating keV electrons is observed to be very low (Figure 1). The buoyant force from ionospheric electrons heated by the precipitating energy can initiate the ionospheric O$^+$ upflows (Hasegawa, 1976; Chaston et al., 2007a).

The DAWs can continue to accelerate and lift the upflowing ions from the ionosphere all the way to the magnetosphere at all local times (Figure 6), even directly pumping them into the ring current region, if on the closed field line region (Chaston et al., 2016). Multiple-satellite observations by Zhang H et al. (2022) demonstrated that a highway, in terms of its high efficiency of O$^+$ transport, forms on the closed field lines and that the O$^+$ ions are accelerated repeatedly near the equator by DAWs to create counter-streaming beams and to enhance the partial ring current. In this study, only O$^+$ beams inside the IVOCs are observed on the closed field lines; no counter-streaming beam is observed, indicating that the ions may continue to be accelerated nonadiabatically upward at altitudes beyond ~5 R_E and that they will never come back even along the closed field lines through adiabatic motion. The DAWs thus appear to be solely responsible for driving the upflows along field lines from the ionosphere to the equator (Figure 6).

The form of the inverted-V structures, i.e., the high-energy O$^+$ ions embraced by the low-energy ions in space, indicates that the magnetospheric convection in these events may not be signifi-
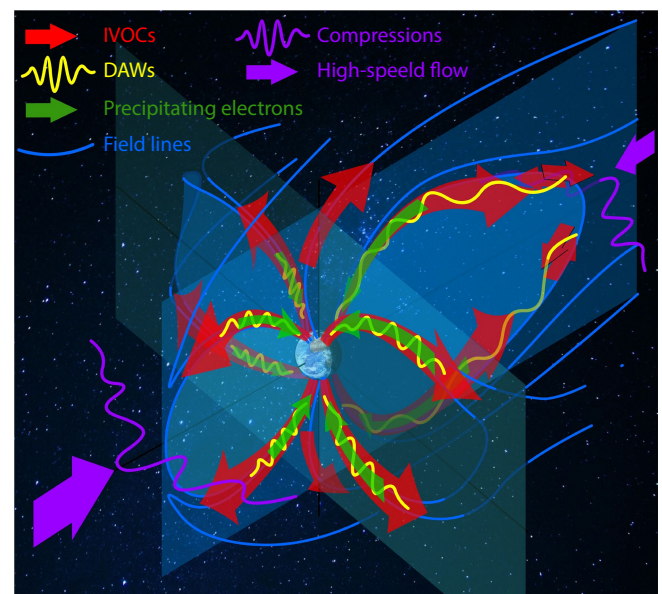

Figure 6. A schematic diagram showing the O$^+$ upflows and the precipitating electrons within the global IVOCs driven by the DAWs that are excited by the compressions from either the magnetopause surface waves or the nightside high-speed flows from mid-tail magnetic reconnection.

cant. Otherwise, the velocity filter effect, i.e., the higher-energy ions always leading the low energy ions in altitudes within a flux tube that is moving with the convection, will be very clear (Horwitz, 1986; Dubouloz et al., 1998), and there will be no invert-V structure. Figure 7 shows two diagrams of upflows of O$^+$ ions locally accelerated with (Panel 7a) and without (Panel 7b) magnetospheric convection. These diagrams are modified from Fig. 1 of Bouhram et al. (2004) by taking into account the fact that ions' drift velocities with electric field (magnetospheric convection) are energy-independent whereas their field-aligned upward velocities are altitude-dependent (increasing with height) because of the pitch angle folding by the mirror force over the polar ionosphere regions (thus, the transversal acceleration cannot change the direction of the trajectory of the guide center of an oxygen ion undergoing the electric field drift, whereas the magnetic mirror force can). If the magnetospheric convection is significant, as shown in Panel 7a, satellites will observe different energy-spectrum structures at different altitudes. At low altitudes, an inverted-V structure can be obtained (the sketched energy-time spectra at right bottom of Panel 7a) since the less-accelerated ions can reach the low-altitude satellite at both the leading and trailing edges of the moving flux tube. Bouhram et al. (2004) have used this low-altitude picture to interpret the inverted-V structure observed. At low satellite altitudes, if the acceleration region is limited below the satellite's trajectory, both heated and unheated ionospheric ions will be recorded simultaneously in the data (not shown in Figure 7). At high altitudes, however, energy dispersion will be seen in energy spectra plots; the high-energy or low-energy ions will be detected first depending on how the observing satellite traverses the structure. In this study, the heights of all the observed IVOCs are at least 5 R_E; these are not low-altitudes.

Let us consider a normal magnetospheric convection with electric field of 40 mV/m (Kelley, 1989) that corresponds to a convection velocity of 100 km/s at the height of 5 R_E with magnetic field magnitude of 400 nT, as observed in the three cases in this study. In fact, this convection velocity is even comparable to a thermal velocity (100 km/s) of the 1 keV O$^+$ ions, and it would have produced a clear asymmetric velocity distribution of these ions, which, however, has not been seen at different altitudes, for example, in Fig. 2 of Bouhram et al. (2004). The 10 eV low-energy O$^+$ ions at the leading and trailing edges of the IVOCs are of the upflowing velocities of 10 km/s, and they take ~45 minutes to travel from the ionosphere to the height of the observing satellite, during which, however, the flux tube along which these 10 eV O$^+$ ions drift must have moved tailward for ~40 R_E, a distance much longer than the width of the upflow channels (~1 R_E) observed in this study; moreover, the 1 keV O$^+$ ions must have passed the satellite's trajectory much earlier and much more upstream, which cannot be embraced by the 10 eV ions in space at the altitude of the satellite's trajectory. Fast convection is thus not the case in this study.

However, if the magnetospheric convection is so small that it can be neglected, the inverted-V structure will be easily formed in the energy spectra at the 5 R_E altitudes, as shown in Panel 7b, even if the acceleration region (the free energy region) extends above or is limited below the trajectory of the observing satellite. In fact, the left plots in Panels 2a and 2c in Figure 2 show that the accelerated ions are of pitch angles even larger than 60°, indicating that these ions are being accelerated — or are at least are not far away from the acceleration region, below, along the magnetic field lines. The convection is weak probably because the locations of the wave-associated IVOCs are near the open-closed field line boundary, and it can be significant in the polar caps away from the open-closed field line boundaries. For the dawnside case reported in this study, even if the magnetospheric convection were strong, the velocity filter effect would have spread the ions
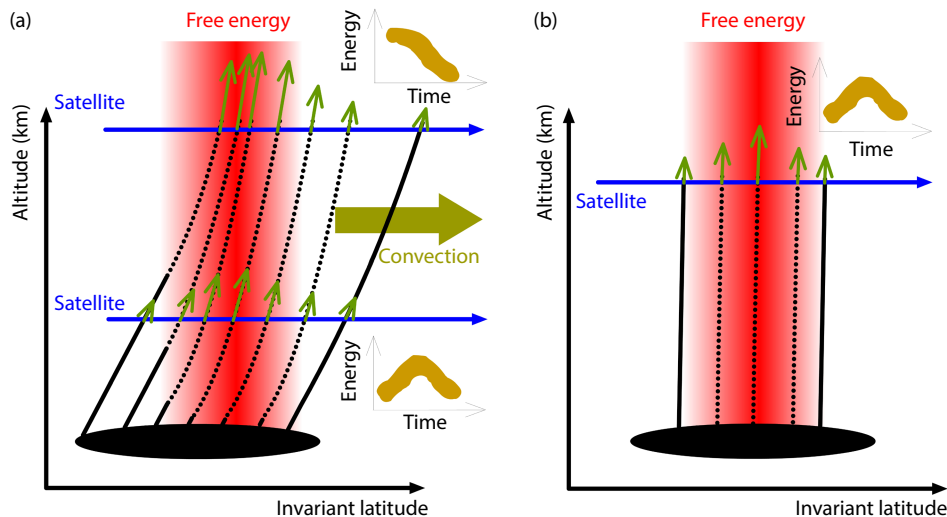
Figure 7. The sketches describing the energization of O$^+$ ions (a) with and (b) without magnetospheric convection. The red region is of free energy that is provided by the DAWs in this study that can heat the O$^+$ ions mainly perpendicularly. The black curves show the trajectories of the ions' guide centers, which are determined by the ions' parallel velocities and the convection velocity (the solid portions of curves denote the unheated ionospheric ions, and the dotted curves denote the heated ions). The green arrows at the ends of the ions' trajectories show the direction and magnitude of the velocities of the ions' guide centers. The horizontal blue arrows show trajectories of the observing satellite at the different altitudes, which detect different energy-time spectra of the O$^+$ ions.

along the tailward direction. The observing satellite C3/Cluster, however, traversed the ion acceleration region flankward, in a direction perpendicular to the convection; yet it still obtained the inverted-V structure, indicating that the acceleration source is not located in the middle of the inverted-V structures, at least not for the flank cases.

In the polar caps with MLats beyond 80°, however, the waves are weak and the IVOCs are also observed (Panel 5a in Figure 5). The ion energies inside these high-latitude IVOCs are systematically lower than the low-latitude ones. These high-latitude and high-altitude IVOCs (Panel 5a in Figure 5) have moved away from the acceleration regions because of the fast convection in the polar caps, and the acceleration source may also have been weakened with time or at large altitudes. The higher-energy O^+ ions have either escaped to the larger heights from the upstream region or have drifted out of the flux tube (not electric field drift), both because of their higher energies, and only the lower-energy O^+ ions are left.

The differential O^+ fluxes inside these IVOCs reach $\sim 10^7$ 1 cm^{-2} s^{-1} sr^{-1} keV^{-1} (Panels f–h in Figures 1, 3 and 4), as large as those inside the extreme case reported by Zhang H et al. (2022). The frequent occurrence of the IVOCs both in time and in space and the high efficiency of O^+ transport inside (Figures 1f–1g and Figure 3b), both denote that the IVOCs simply driven by the DAWs are of great importance for mass and energy exchange during the ionosphere–magnetosphere coupling (Figure 6).

6. Summary

In this study, large-scale ($\sim R_E$) IVOCs are identified in ion energy spectrum data collected by Cluster. These frequently-detected structures are found to be closely associated with DAWs in MLats below 80°, near the open-closed field line boundary, which establish transport channels to accelerate the oxygen ions and to lift them up. The PEFs of the DAWs precipitate the aurora electrons (>1 keV), which may initiate the O^+ upflows in the top ionosphere. The upflowing O^+ ions in the center of the IVOCs are then accelerated by the DAWs both perpendicularly and parallelly, which accounts for the observed inverted-V energy spectra. These inverted-V structures themselves indicate that the magnetospheric convection may be weak inside these channels. The DAWs provide a simple but efficient way to drive the oxygen upflows widely from the polar regions of the ionosphere towards the magnetosphere (Figure 6), and the IVOCs thus manifest this global pumping process.

Open Research

Acknowledgments

References

Archer, M. O., Hietala, H., Hartinger, M. D., Plaschke, F., and Angelopoulos, V. (2019). Direct observations of a surface eigenmode of the dayside magnetopause. *Nat. Commun.*, *10*(1), 615. https://doi.org/10.1038/s41467-018-08134-5

Axford, W. I. (1968). The polar wind and the terrestrial helium budget. *J. Geophys. Res.*, *73*(21), 6855–6859. https://doi.org/10.1029/JA073i021p06855

Balogh, A., Carr, C. M., Acuña, M. H., Dunlop, M. W., Beek, T. J., Brown, P., Fornacon, K. H., Georgescu, E., Glassmeier, K. H., … Schwingenschuh, K. (2001). The cluster magnetic field investigation: Overview of in-flight performance and initial results. *Ann. Geophys.*, *19*(10-12), 1207–1217. https://doi.org/10.5194/angeo-19-1207-2001

Bostrom, R. (1992). Observations of weak double layers on auroral field lines. *IEEE Trans. Plasma Sci.*, *20*(6), 756–763. https://doi.org/10.1109/27.199524

Bouhram, M., Klecker, B., Miyake, W., Rème, H., Sauvaud, J. A., Malingre, M., Kistler, L., and Blăgău, A. (2004). On the altitude dependence of transversely heated O^+ distributions in the cusp/cleft. *Ann. Geophys.*, *22*(5), 1787–1798. https://doi.org/10.5194/angeo-22-1787-2004

Brambles, O. J., Lotko, W., Zhang, B., Wiltberger, M., Lyon, J., and Strangeway, R. J. (2011). Magnetosphere sawtooth oscillations induced by ionospheric outflow. *Science*, *332*(6034), 1183–1186. https://doi.org/10.1126/science.1202869

Chappell, C. R. (1988). The terrestrial plasma source: a new perspective in solar-terrestrial processes from dynamics explorer. *Rev. Geophys.*, *26*(2), 229–248. https://doi.org/10.1029/RG026i002p00229

Chaston, C. C., Bonnell, J. W., Carlson, C. W., McFadden, J. P., Ergun, R. E., Strangeway, R. J., and Lund, E. J. (2004). Auroral ion acceleration in dispersive Alfvén waves. *J. Geophys. Res.: Space Phys.*, *109*(A4), A04205. https://doi.org/10.1029/2003ja010053

Chaston, C. C., Peticolas, L. M., Carlson, C. W., McFadden, J. P., Mozer, F., Wilber, M., Parks, G. K., Hull, A., … Acuña, M. A. (2005). Energy deposition by Alfvén waves into the dayside auroral oval: Cluster and FAST observations. *J. Geophys. Res.: Space Phys.*, *110*(A2), A02211. https://doi.org/10.1029/2004ja010483

Chaston, C. C., Carlson, C. W., McFadden, J. P., Ergun, R. E., and Strangeway, R. J. (2007a). How important are dispersive Alfvén waves for auroral particle acceleration?. *Geophys. Res. Lett.*, *34*(7), L07101. https://doi.org/10.1029/2006gl029144

Chaston, C. C., Wilber, M., Mozer, F. S., Fujimoto, M., Goldstein, M. L., Acuna, M., Reme, H., and Fazakerley, A. (2007b). Mode conversion and anomalous transport in Kelvin-Helmholtz vortices and kinetic Alfvén waves at the earth's magnetopause. *Phys. Rev. Lett.*, *99*(17), 175004. https://doi.org/10.1103/PhysRevLett.99.175004

Chaston, C. C., Bonnell, J. W., Wygant, J. R., Mozer, F., Bale, S. D., Kersten, K., Breneman, A. W., Kletzing, C. A., Kurth, W. S., … MacDonald, E. A. (2014). Observations of kinetic scale field line resonances. *Geophys. Res. Lett.*, *41*(2), 209–215. https://doi.org/10.1002/2013gl058507

Chaston, C. C., Bonnell, J. W., Kletzing, C. A., Hospodarsky, G. B., Wygant, J. R., and Smith, C. W. (2015a). Broadband low-frequency electromagnetic waves in the inner magnetosphere. *J. Geophys. Res.: Space Phys.*, *120*(10), 8603–8615. https://doi.org/10.1002/2015ja021690

Chaston, C. C., Bonnell, J. W., Wygant, J. R., Kletzing, C. A., Reeves, G. D., Gerrard, A., Lanzerotti, L., and Smith, C. W. (2015b). Extreme ionospheric ion energization and electron heating in Alfvén waves in the storm time inner magnetosphere. *Geophys. Res. Lett.*, *42*(24), 10531–10540. https://doi.org/10.1002/2015gl066674

Chaston, C. C., Bonnell, J. W., Reeves, G. D., and Skoug, R. M. (2016). Driving ionospheric outflows and magnetospheric O^+ energy density with Alfvén waves. *Geophys. Res. Lett.*, *43*(10), 4825–4833. https://doi.org/10.1002/2016gl069008

Chen, L., Lin, Z. H., and White, R. (2001). On resonant heating below the cyclotron frequency. *Phys. Plasmas*, 8(11), 4713–4716. https://doi.org/10.1063/1.1406939

Cornilleau-Wehrlin, N., Chauveau, P., Louis, S., Meyer, A., Nappa, J. M., Perraut, S., Rezeau, L., Robert, P., ... Louarn, H. (1997). The Cluster spatio-temporal analysis of field fluctuations (STAFF) experiment. *Space Sci. Rev.*, 79(1-2), 107–136. https://doi.org/10.1023/a:1004979209565

Cui, Y. B., Fu, S. Y., and Parks, G. K. (2014). Heating of ionospheric ion beams in inverted-V structures. *Geophys. Res. Lett.*, 41(11), 3752–3758. https://doi.org/10.1002/2014gl060524

Dubouloz, N., Delcourt, D., Malingre, M., Berthelier, J. J., and Chugunin, D. (1998). Remote analysis of cleft ion acceleration using thermal plasma measurements from Interball Auroral Probe. *Geophys. Res. Lett.*, 25(15), 2925–2928. https://doi.org/10.1029/98gl02181

Escoubet, C. P., Fehringer, M., and Goldstein, M. (2001). *Introduction* The Cluster mission. *Ann. Geophys.*, 19(10-12), 1197–1200. https://doi.org/10.5194/angeo-19-1197-2001

Fu, S. Y., Zong, Q. G., Fritz, T. A., Pu, Z. Y., and Wilken, B. (2002). Composition signatures in ion injections and its dependence on geomagnetic conditions. *J. Geophys. Res.: Space Phys.*, 107(A10), SMP 14-1-SMP 14-16. https://doi.org/10.1029/2001ja002006

Gkioulidou, M., Ohtani, S., Ukhorskiy, A. Y., Mitchell, D. G., Takahashi, K., Spence, H. E., Wygant, J. R., Kletzing, C. A., and Barnes, R. J. (2019). Low-energy (< keV) O^+ ion outflow directly into the inner magnetosphere: Van Allen Probes observations. *J. Geophys. Res.: Space Phys.*, 124(1), 405–419. https://doi.org/10.1029/2018ja025862

Gustafsson, G., André, M., Carozzi, T., Eriksson, A. I., Fälthammar, C. G., Grard, R., Holmgren, G., Holtet, J. A., Ivchenko, N., ... Wahlund, J. E. (2001). First results of electric field and density observations by Cluster EFW based on initial months of operation. *Ann. Geophys.*, 19(10-12), 1219–1240. https://doi.org/10.5194/angeo-19-1219-2001

Hasegawa, A. (1976). Particle acceleration by MHD surface wave and formation of aurora. *J. Geophys. Res.*, 81(28), 5083–5090. https://doi.org/10.1029/JA081i028p05083

Horwitz, J. L. (1986). Velocity filter mechanism for ion bowl distributions (bimodal conics). *J. Geophys. Res.: Space Phys.*, 91(A4), 4513–4523. https://doi.org/10.1029/JA091iA04p04513

Johnstone, A. D., Alsop, C., Burge, S., Carter, P. J., Coates, A. J., Coker, A. J., Fazakerley, A. N., Grande, M., Gowen, R. A., ... Woodliffe, R. D. (1997). Peace: A plasma electron and current experiment. *Space Sci. Rev.*, 79(1-2), 351–398. https://doi.org/10.1023/a:1004938001388

Kelley, M. C. (1989). High-latitude electrodynamics. In M. C. Kelley (Ed.), *The Earth's Ionosphere: Plasma Physics and Electrodynamics* (pp. 381). San Diego: Elsevier Inc. https://doi.org/10.1016/B978-0-12-404013-7.50011-3

Klumpar, D. M., Peterson, W. K., and Shelley, E. G. (1984). Direct evidence for two-stage (bimodal) acceleration of ionospheric ions. *J. Geophys. Res.: Space Phys.*, 89(A12), 10779–10787. https://doi.org/10.1029/JA089iA12p10779

Kronberg, E. A., Ashour-Abdalla, M., Dandouras, I., Delcourt, D. C., Grigorenko, E. E., Kistler, L. M., Kuzichev, I. V., Liao, J., Maggiolo, R., ... Zelenyi, L. M. (2014). Circulation of heavy ions and their dynamical effects in the magnetosphere: recent observations and models. *Space Sci. Rev.*, 184(1-4), 173–235. https://doi.org/10.1007/s11214-014-0104-0

Lui, A. T. Y. (1993). Radial transport of storm time ring current ions. *J. Geophys. Res.: Space Phys.*, 98(A1), 209–214. https://doi.org/10.1029/92ja02079

Norqvist, P., André, M., and Tyrland, M. (1998). A statistical study of ion energization mechanisms in the auroral region. *J. Geophys. Res.: Space Phys.*, 103(A10), 23459–23473. https://doi.org/10.1029/98ja02076

Réme, H., Aoustin, C., Bosqued, J. M., Dandouras, I., Lavraud, B., Sauvaud, J. A., Barthe, A., Bouyssou, J., Camus, T., ... Sonnerup, B. (2001). First multispacecraft ion measurements in and near the Earth's magnetosphere with the identical Cluster ion spectrometry (CIS) experiment. *Ann. Geophys.*, 19(10-12), 1303–1354. https://doi.org/10.5194/angeo-19-1303-2001

Schuck, P. W., Bonnell, J. W., and Kintner, P. M. (2003). A review of lower hybrid solitary structures. *IEEE Trans. Plasma Sci.*, 31(6), 1125–1177. https://doi.org/10.1109/tps.2003.822043

Shelley, E. G., Peterson, W. K., Ghielmetti, A. G., and Geiss, J. (1982). The polar ionosphere as a source of energetic magnetospheric plasma. *Geophys. Res. Lett.*, 9(9), 941–944. https://doi.org/10.1029/GL009i009p00941

Stasiewicz, K., Bellan, P., Chaston, C., Kletzing, C., Lysak, R., Maggs, J., Pokhotelov, O., Seyler, C., Shukla, P., ... Wahlund, J.-E. (2000a). Small scale Alfvénic structure in the aurora. *Space Sci. Rev.*, 92(3-4), 423–533. https://doi.org/10.1023/a:1005207202143

Stasiewicz, K., Khotyaintsev, Y., Berthomier, M., and Wahlund, J. E. (2000b). Identification of widespread turbulence of dispersive Alfvén waves. *Geophys. Res. Lett.*, 27(2), 173–176. https://doi.org/10.1029/1999gl010696

Stasiewicz, K., Lundin, R., and Marklund, G. (2000c). Stochastic ion heating by orbit chaotization on electrostatic waves and nonlinear structures. *Phys. Scr.*, 2000(T84), 60–63. https://doi.org/10.1238/Physica.Topical.084a00060

Strangeway, R. J., Ergun, R. E., Su, Y. J., Carlson, C. W., and Elphic, R. C. (2005). Factors controlling ionospheric outflows as observed at intermediate altitudes. *J. Geophys. Res.: Space Phys.*, 110(A3), A03221. https://doi.org/10.1029/2004ja010829

Tsyganenko, N. A., and Sitnov, M. I. (2005). Modeling the dynamics of the inner magnetosphere during strong geomagnetic storms. *J. Geophys. Res.: Space Phys.*, 110(A3), A03208. https://doi.org/10.1029/2004ja010798

Wang, Z. Q., Pan, Z. R., Zhai, H., Gao, Z. X., Sun, K., and Zhang, Y. S. (2017). The nonlinear interactions between O^+ ions and oxygen band EMIC waves. *J. Geophys. Res.: Space Phys.*, 122(7), 7097–7109. https://doi.org/10.1002/2017ja024113

Welling, D. T., André, M., Dandouras, I., Delcourt, D., Fazakerley, A., Fontaine, D., Foster, J., Ilie, R., Kistler, L., ... Yau, A. (2015). The earth: plasma sources, losses, and transport processes. *Space Sci. Rev.*, 192(1-4), 145–208. https://doi.org/10.1007/s11214-015-0187-2

Yau, A. W., and André, M. (1997). Sources of ion outflow in the high latitude ionosphere. *Space Sci. Rev.*, 80(1-2), 1–25. https://doi.org/10.1023/a:1004947203046

Young, D. T. (1986). Experimental aspects of ion acceleration in the earth's magnetosphere. In T. Chang, et al. (Eds.), *Ion Acceleration in the Magnetosphere and Ionosphere* (pp. 17-35). Washington: American Geophysical Union. https://doi.org/10.1029/GM038p0017

Zhang, H., Fu, S. Y., Pu, Z. Y., Lu, J. Y., Zhong, J., Zhu, C. B., Wan, W. X., and Liu, L. B. (2019). Statistics on the magnetosheath properties related to magnetopause magnetic reconnection. *Astrophys. J.*, 880(2), 122. https://doi.org/10.3847/1538-4357/ab290e

Zhang, H., Fu, S. Y., Fu, S., Zhong, J., Ni, B. B., Wei, Y., Pu, Z. Y., Chen, Y. D., Ge, Y. S., ... Liu, L. B. (2022). A highway for atmospheric ion escape from earth during the impact of an interplanetary coronal mass ejection. *Astrophys. J.*, 937(1), 4. https://doi.org/10.3847/1538-4357/ac8a93

Zhao, K., Kistler, L. M., Lund, E. J., Nowrouzi, N., Kitamura, N., and Strangeway, R. J. (2020). Factors controlling O^+ and H^+ outflow in the cusp during a geomagnetic storm: FAST/TEAMS observations. *Geophys. Res. Lett.*, 47(11), e2020GL086975. https://doi.org/10.1029/2020gl086975

Zong, Q. G., Wang, Y. F., Zhang, H., Fu, S. Y., Zhang, H., Wang, C. R., Yuan, C. J., and Vogiatzis, I. (2012). Fast acceleration of inner magnetospheric hydrogen and oxygen ions by shock induced ULF waves. *J. Geophys. Res.: Space Phys.*, 117(A11), A11206. https://doi.org/10.1029/2012ja018024